Hindawi
Shock and Vibration
Volume 2022, Article ID 3520982, 13 pages
https://doi.org/10.1155/2022/3520982

*Research Article*

# Numerical Simulation of Vortex-Induced Transverse Vibration of a Cylinder with Very Low Mass Ratio

**Xinxing Zhang,[1] Minghan Hu,[2] Jiancheng Cai,[2,3] Andrii Babenko,[2,3] E. Shiju,[2,3] and Zisheng Xu[2,3]**

[1]*School of Mechanical and Electrical Engineering, Quzhou College of Technology, Quzhou 324000, Zhejiang, China*
[2]*College of Engineering, Zhejiang Normal University, Jinhua 321004, China*
[3]*Key Laboratory of Urban Rail Transit Intelligent Operation and Maintenance Technology & Equipment of Zhejiang Province, Jinhua 321005, China*

Correspondence should be addressed to Jiancheng Cai; cai_jiancheng@foxmail.com

Received 16 July 2022; Revised 7 September 2022; Accepted 15 September 2022; Published 4 October 2022

Academic Editor: Madalina Dumitriu



Vortex-induced vibration (VIV) of flow past different types of cylinders is important in many engineering fields and has led to a large number of fundamental studies. Computational fluid dynamics (CFD) has become a powerful tool to investigate VIV problems. In this paper, the VIV of an elastically supported rigid-body circular cylinder was numerically studied by solving the Reynolds-averaged Navier–Stokes (RANS) equations with the shear stress transport (SST) $k$-$\omega$ turbulence model. The dynamic mesh approach was used to tackle the domain mesh change due to the cylinder motion. The characteristics of the amplitude response of the cylinder and the vortex shedding frequency at different reduced velocities were compared with the experimental data, and good agreement was found regarding the vibration amplitude and the frequency lock-in phenomenon. Results show the influence of added mass was perceptible in the free vibration and in the initial branch with small cylinder vibration amplitude, while it is fairly weak in the upper and lower branches considering the fact that the main response frequency of the cylinder is close to the natural frequency in a vacuum. Detailed vorticity distributions clearly indicate the 2P vortex modes at the upper and lower branches, and the 2S mode at the initial branch and their generation mechanisms are analyzed. The effects of the cylinder vibration on the lift and drag forces at different branches are discussed, and the frequencies of peak values in their Fourier spectra are examined. The phase difference between the lift force and the cylinder vibration shows an obvious jump from the initial branch to the upper branch with the vortex mode switching from 2S to 2P.

## 1. Introduction

Vortex-induced vibration (VIV) of flow past bluff bodies is part of a number of disciplines involving fluid mechanics, structural mechanics, vibrations, computational fluid dynamics (CFD), acoustics, wavelet transforms, and smart materials [1]. Among them, flow past cylinders is often encountered in many fields such as aerospace, nuclear engineering, wind engineering, marine engineering, construction engineering, ground transportation, and sports. VIV should be avoided in most cases of structural safety, as pointed in [2]; the vibrations of small amplitude may lead to fatigue or fretting wear in the long term, while for large amplitude vibration, the damage may occur in the short term. On the other hand, VIV can be used for energy harvesting [3–5]. Early experimental results on the characteristics of lift, drag, and dimensionless frequency of vortex shedding (Strouhal number) for the flow around a stationary cylinder, such as Achenbach [6, 7], Cantwell and Coles [8], and Schewe [9], have been well summarized in the monographs of Sumer and Fredsoe [10] and Zdravkovich [11, 12].

The most interesting phenomena of flow past a cylinder are vortex shedding. Its frequency $f_{vs}$ for a stationary cylinder $f_{vs}$ follows Strouhal's law, i.e., $f_{vs} = St \cdot U/D$, with $U$ being the flow incoming velocity and $D$ being the cylinder

diameter. The Reynolds number, defined as $\mathrm{Re_D} = \rho UD/\mu$ with $\rho$ and $\mu$ being the density and dynamic viscosity of the fluid, respectively, is used to describe the flow regime. In the subcritical regime, with $300 < \mathrm{Re_D} < 3 \times 10^5$, the wake flow is turbulent while the boundary layer over the cylinder surface remains laminar, and $St \approx 0.2$ for circular cylinders.

When the cylinder moves in either predetermined forced vibration or flow-induced vibration, the situation will become more complex due to the interactions between vortex motions and cylinder vibrations. The vortex motion may change with the vibration of the cylinder, and vice versa, in the case of VIV. With low incoming velocity, the vortex-shedding frequency obeys the stationary-cylinder Strouhal frequency until the reduced velocity $U_r$ (its definition is given in the next section) approaches the value of 5. With a further increase in the velocity beyond this point, however, it departs from the Strouhal frequency and begins to follow the natural frequency of the system, remains locked into the natural frequency of the system at $U_r = 5$, and remains locked in until $U_r$ reaches the value of about 7 [10]. This phenomenon is known as the "lock-in" or "synchronization" phenomenon, which is characterized by strong fluid-structure interaction.

Although there are different cross-section shapes of cylinders as well as the boundary conditions, the elastically supported circular cylinders are the most fundamental cases. In the study of VIVs of elastically supported cylinders, Feng [13] experimentally investigated the VIV of elastically supported one-degree-of-freedom (1DOF) rigid circular and D-shape cylinders with a large mass ratio $m^*$ (ratio of the cylinder mass with displaced fluid mass) in detail in the transverse direction in a wind tunnel and found that when the vortex-induced frequency is close to the natural frequency of the cylinder structure, the cylinder amplitude increases dramatically and the "lock-in" phenomenon will occur, so that the cylinder vibration system can effectively obtain energy from the fluid. Khalak and Williamson [14–17] measured the VIVs of a cylinder with a low mass and damping ratio. By checking the relationship curve between the maximum vibration amplitude and the reduced velocity, they divided the amplitude response into three regions, namely, the initial branch, the upper branch, and the lower branch. The upper branch is absent in large $m^*$ cases, such as in the study by Feng [13]. Khalak and Williamson [16] also found that for the upper and lower branches with large cylinder vibration amplitude, the wake vortex distribution is 2P modes, while the initial branch with small amplitude is 2S modes. In the 2P mode, two pairs of vortices generate in opposite directions in one cycle of cylindrical vibration, while in the 2S mode, there are two independent vortices in one cycle of cylindrical vortex-induced vibration.

In the numerical study of VIVs of elastically supported cylinders, Bahmani and Akbari [18] investigated the dynamic response and vortex shedding of an elastically mounted circular cylinder with $\mathrm{Re_D}$ ranging from 80 to 160 and found that for $m^* = 74.5$ and 149, lock-in had occurred but not in the case of $m^* = 298$. Only the 2S vortex shedding mode was observed at these low Reynolds numbers, in contrast to the 2P mode of vortex shedding in the turbulent flow regime during lock-in. Li et al. [19], referring to the experimental results of Khalak and Williamson [14], carried out two-dimensional flow field calculations with $K$-$\varepsilon$ and shear stress transport (SST) $K$-$\omega$ turbulence models and found that the SST $K$-$\omega$ model is more appropriate for the simulation of VIV of the elastically mounted rigid cylinder, comparing the cylinder vibration amplitudes with the experimental data, and can successfully capture the 2P wake mode in the upper branch. Guilmineau and Queutey [20] simulated the VIV experiments conducted by Khalak and Williamson [14] with SST $K$-$\omega$ turbulence models with $\mathrm{Re_D}$ in the range of 900–15 000 and $U_r$ between 1.0 and 17.0 and discussed the influence of initial conditions on predicting the maximum amplitude correctly. Results show that under the rest and decreasing velocity conditions, the simulations successfully predict only the lower branch, while with the increasing velocity condition, the maximum vibration amplitude corresponds to the experimental value, although the upper branch does not match experimental data. Pan et al. [21] also employed the two-dimensional numerical simulations of the VIV of an elastically supported cylinder with an SST $K$-$\omega$ turbulence model and discussed the influence of random disturbance on VIV characteristics between experimental and numerical results, and they found different 2P modes reproduced in the simulations were consistent with the experimental results in the upper and lower branches. Khan et al. [22] also made similar simulations of the experimental results of Khalak and Williamson [14] and found that the cylinder vibration amplitude and drag forces are small in the initial branch, and the maximum displacement response of the cylinder is located in the upper branch, with the corresponding dimensionless velocity, which is greater than the experimental results.

Sayyaadi and Motekallem [23] carried out a three-dimensional simulation of the vortex-induced transverse and inline vibrations of three elastic cylinders in a regular triangle arrangement at $\mathrm{Re_D} > 4 \times 10^5$ and found that the inline amplitude of downstream cylinders could be as large as $0.54D$, while the maximum transverse amplitude of three cylinders can reach up to $2.30D$. Kinaci [24] argued that 2D simulations provide a fast solution to such a complex flow phenomenon although it is not possible to capture the tip effects of VIV of the elastically supported cylinder and found that the maximum amplitude achieved by the cylinder in the upper branch was not captured with CFD with the $K$-$\omega$ turbulence model as was also mentioned in [20, 21]. Recently, Mutlu et al. [25] also numerically investigated the VIV of a smooth cylinder for the transition of shear layer type 2 flow using the SST $K$-$\omega$ turbulence model for the 2D approach and practically discussed the effects of four different mass-damping ratios on the vibration amplitude of the one-degree-of-freedom of the cylinder reveal. They found that there is an inverse correlation between the mass-damping ratios and the transition from the upper to the lower branch.

As pointed out in [25], many past studies dealt with the VIV of flow past a cylinder with high or moderate mass-damping ratios, but only a few studies have considered the effects of a low mass-damping ratio so far. Therefore, it is still

an open topic in this area, especially in the high Reynolds range, such as the influences of the cylinder vibration on the lift and drag forces in each branch and the formation mechanisms of the different vortex modes. The present work numerically studied the vortex induced transverse vibration of an elastically supported cylinder with a very low mass-damping ratio, i.e., the mass ratio $m^* = 2.4$, the damping ratio $\zeta = 0.0054$, and the Reynolds number $\mathrm{Re_D}$ ranged from $2.74 \times 10^4$ to $1.43 \times 10^5$. Experimental data of the VIVs obtained in the cross-flow direction of an elastically supported cylinder with low mass and damping ratios can be found in the study by Khalak and Williamson [14–17], so that the validation of the present study can be realized by comparing the numerical results with the experimental ones.

The unsteady Reynolds-averaged Navier–Stokes equations (URANS) with the SST $k$-$\omega$ turbulence model approach was employed to solving the flow fields, and dynamic mesh technique, specifically the smoothing technique of mesh displacement diffusion method, was used to update the computational grids according to cylinder motion response. The free vibration of the cylinder was simulated first to check the numerical accuracy and the influence of the added mass on the natural frequency. The characteristics of the amplitude response of the cylinder with the influence from the added mass, the vortex shedding frequency, and the fluctuating lift and drag forces at different reduced velocities are explored. Detailed vorticity distributions are examined to show the mechanisms of the 2P and 2S modes.

## 2. Materials and Methods

*2.1. Mathematical Model.* The elastically supported 1DOF circular cylinder is schematically shown in Figure 1 with the cylinder mass $m$, the spring coefficient $k$, and the damping coefficient $c$. The cylinder diameter $D = 0.1$ m. The mass ratio $m^* = m_s/(\rho\pi D^2/4) = 2.4$, which is equal to the experiment parameter in [14]. The structural equation of vibration of the elastically mounted cylinder, which allows it to vibrate in the transverse $y$ direction is

$$m_s\ddot{y} + c\dot{y} + ky = F_L(y, \dot{y}, t) = 0.5C_L\rho DU, \tag{1}$$

where $F_L(y, \dot{y}, t)$ is the aerodynamic lift force, which is related to the cylinder transverse displacement $y$ and velocity $\dot{y}$, $C_L$ is the lift force coefficient, $U$ is the incoming flow velocity, and $\rho$ is the density of the fluid. Lift force which causes cylinder motion can be obtained based on pressure distribution integration over cylinder surface. The mathematical method of solution of differential equations (1) to obtain a cylinder displacement value in $y$ direction during each time step is presented in Section 2.2.

The natural frequency of the cylinder vibration system without the damping in vacuum is $f_0 = \sqrt{k/m}/2\pi$. In this work, we tuned $k$ and $m$ so that $f_0 = 15$Hz. If the added mass $m_A = \rho\pi D^2/4$ using the potential flow theory is taken into account, then the natural frequency of the vibration system is $f_N = \sqrt{k/(m + m_A)}/2\pi$. It can be seen that with a small value of the mass ratio $m^*$, the added mass $m_A$ has a great influence on the natural frequency of the vibration system. Specifically, with $m^* = 2.4$, $f_N = 12.6$ Hz here. The dimensionless damping ratio $\zeta = 0.0054$ is selected according to the experiment parameter value in [26].

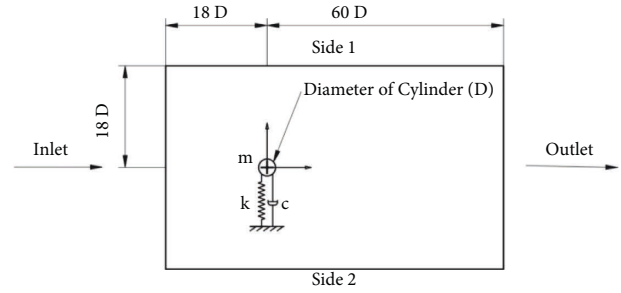


Figure 1: Schematic view of vortex-induced vibration of the elastically supported cylinder.

With the vortex shedding frequency of flow past a stationary cylinder $f_{vs}$, the Strouhal number as the nondimensional vortex shedding frequency is defined as

$$St = f_{vs}\frac{D}{U}, \tag{2}$$

and the nondimensional reduced velocity $U_r$ is defined as follows:

$$U_r = \frac{U}{(f_N D)}, \tag{3}$$

In the study, the characteristic Mach number value corresponding to the incoming flow velocity is much less than 0.3, so that the flow can be considered as incompressible. The continuity equation and momentum equation of incompressible flow can form a closed problem mathematically without adding and solving the energy equation. The characteristic Reynolds number $\mathrm{Re_D}$ in the simulations ranges from $2.74 \times 10^4$ to $1.43 \times 10^5$ so that flow is in turbulent regime. The unsteady RANS equations with the SST $K$-$\omega$ turbulence model by Menter [27] were solved.

The Reynolds averaged continuity equation and momentum equation (Navier–Stokes equation) are as follows [27]:

$$\nabla \cdot \overline{\mathbf{u}} = 0, \tag{4}$$

$$\frac{\partial \overline{\mathbf{u}}}{\partial t} + \nabla \cdot (\overline{\mathbf{u}}\overline{\mathbf{u}}) = -\frac{1}{\rho}\nabla\overline{p} + \nu\nabla^2\overline{\mathbf{u}} - \frac{1}{\rho}\nabla \cdot \boldsymbol{\tau}^R. \tag{5}$$

The overbar is the ensemble average procedure in the URANS approach. In the equations (4) and (5) $\mathbf{u}$ is the fluid velocity vector and $\tau^R$ is the turbulent or Reynolds stress tensor. By the Boussinesq assumption,

$$\boldsymbol{\tau}^R = \rho\overline{\mathbf{u}'\mathbf{u}'} = 2\mu_T\overline{\mathbf{S}} - \frac{2}{3}\rho K\mathbf{I}, \tag{6}$$

with $\overline{\mathbf{S}}$ the mean strain rate tensor, $\mu_T$ the turbulent eddy viscosity, $K$ the turbulent kinetic energy, and $\mathbf{I}$ the identity tensor.

The transport equations for the turbulent kinetic energy $K$ and turbulent specific dissipation rate $\omega$ in the SST model are described as

$$\frac{\partial \rho K}{\partial t} + \frac{\partial}{\partial x_i}(\rho u_i K) = G_K - \rho c_\mu K\omega + \frac{\partial}{\partial x_j}\left[\left(\mu + \frac{\mu_t}{\sigma_K}\right)\frac{\partial K}{\partial x_j}\right], \quad (7)$$

$$\frac{\partial \rho \omega}{\partial t} + \frac{\partial}{\partial x_i}(\rho u_i \omega) = \alpha \frac{\omega}{K} G_K - \rho\beta\omega^2 + \frac{\partial}{\partial x_i}\left[\left(\mu + \frac{\mu_t}{\sigma_\omega}\right)\frac{\partial \omega}{\partial x_j}\right] + (1 - F_1)\frac{2\rho}{\sigma_{\omega,2}}\frac{1}{\omega}\frac{\partial K}{\partial x_j}\frac{\partial \omega}{\partial x_j}, \quad (8)$$

where $G_K$ represents the generation of turbulence kinetic energy due to mean velocity gradients, $c_\mu$, $\sigma_K$, $\alpha$, $\beta$, $\sigma_\omega$, and $\sigma_{\omega,2}$ are the model tuning parameters, and $F_1$ the blending function. The turbulent viscosity $\mu_t$ is finally defined as follows:

$$\mu_T = \frac{\rho a_1 K}{\max\left(a_1\omega, SF_2\right)}, \quad (9)$$

where $a_1$ is another model constant, $S = \sqrt{2\left(\overline{S}_{ij}\overline{S}_{ij}\right)}$ is the second invariant of the strain rate tensor, and $F_2$is a second blending function. Detailed derivation can be found in [27].

*2.2. CFD Model of the Cylinder VIV System.* In consideration of the high computational cost of 3D simulations, 2D calculations were chosen for the present study as in [19, 21, 22]. Pan et al. [21] argued that structural vibration produces a high degree of span-wise correlation, giving rise to nearly 2D flow structures for an elastically mounted cylinder subjected to flow, so that the application of 2D numerical simulations are reasonable. Kinaci [24] also suggests that although it is not possible to capture the tip effects with 2D simulations; nevertheless, it provides a fast and acceptable solution to such a complex flow phenomenon. In 2D simulations, the flow is assumed to be uniform along the spanwise direction (independent of $z$), so that the vortex shedding is uniform along the $z$ direction. The dimensions of the computational domain are shown in Figure 1 with $36D$ in the cross-flow direction, $18D$ upstream, and $60D$ downstream of the cylinder. The domain is larger than that in [19, 21, 22] in order to reduce the influence of the side boundaries.

The calculations were performed in the ANSYS Fluent CFD package, wherein the finite volume method was used to discretize the Reynolds averaged equations (4) and (5) and the turbulent model equations (7) and (8) for $K$ and $\omega$ parameters. The pressure-based solver is used with the pressure-velocity coupling of the SIMPLEC (SIMPLE consistent) scheme, which is an improved SIMPLE (semi-implicit method for the pressure linked equations) algorithm [28]. For the spatial discretization, the gradient terms were discretized with the least square cell-based method, and the pressure equation was discretized with a second-order scheme. The convective terms in the momentum equation and the turbulent model $K$ and $\omega$ equations (7) and (8) were discretized with the second-order upwind technique. The temporal discretization is second-order upwind.

The velocity boundary condition is applied at the inlet boundary, representing the incoming uniform flow as in a wind tunnel. A low turbulent intensity of 1% with a turbulent viscosity ratio of 2% is set at the inlet. An average static pressure of 0 Pa is applied at the outlet boundary. Nonslip wall is set at the cylinder wall, and free slippery wall is applied at the upper and lower sides of the domain.

Quadrilateral mesh cells were used to mesh the computational domain with fine near-wall cell resolution. The mesh independence was checked by increasing the number of cells gradually according to the suggestion in [29], and finally the mesh scheme with a number of 255 102 cells was adopted. Four mesh schemes with element numbers of 64 746, 141 372, 255 102, and 430 192, respectively, were tested. The evolution of cylinder response and the lift force exerted by the fluid with $U_r = 8$ are shown in Figure 2. As it can be seen, the results of the coarse mesh with 64 746 cells have noticeable differences, and the results of 141 372 cells become close to those of the finer cells. The results obtained on grid schemes with 255 102 and 430 192 cells are very close to each other, especially in the steady-state stage after 0.5 s. If the peak-peak value of the cylinder motions in the steady-state stage as the assessment has been taken, and regarding the value from the finest mesh scheme as the precise value, the relative errors of mesh schemes with 64 746, 141 372, 255, and 102 cells are 10.46%, 5.39%, and 1.69%, respectively. So it can be concluded that 255 102 cells are sufficient to obtain the mesh-independent numerical results.

A snapshot of the mesh around the cylinder and in the wake region is shown in Figure 3. The first layer height near the cylinder wall is set to be $10^{-5}D$ and the cell row heights increase gradually with a ratio of 1.02 to ensure that the nondimensional wall distance $y+$ is around 0.01 and very fine resolution of the near wall flow fields can be obtained. The fine mesh was also created in the wake region along the streamwise direction with a cross-flow distance greater than $4D$, considering the vortex motions therein. The time step $\Delta t$ is set to $10^{-5}$ s, considering the minimum size of the first cell level near the cylinder along the flow direction $\Delta x$. For the maximum inlet velocity in the simulation, the Courant–Friedrichs–Lewy condition $U_{\max}\Delta t/\Delta x < 1$ is satisfied.

Due to the cylinder motion, the fluid domain changes and the dynamic grid technique is used to tackle the issue. The boundaries of the domain were set at fixed limits. To apply dynamic mesh technology, a cylinder was defined as a rigid body which was allowed to move in a transverse direction. The fluid domain was specified as the deforming zone. Mesh deformation is determined by unprescribed cylinder motion based on lift force change, which acts on the cylinder.

The aerodynamic force on the cylinder was obtained by the integration of the stress over the cylinder wall, and the transverse force (in the $y$-direction) is the exciting force to the force vibration of the cylinder, as expressed in equation (1). The forced vibration of the cylinder was numerically solved with the Adams–Moulton method [30]. Second-order equation (1) was transformed into a system of two first-order ordinary differential equations:

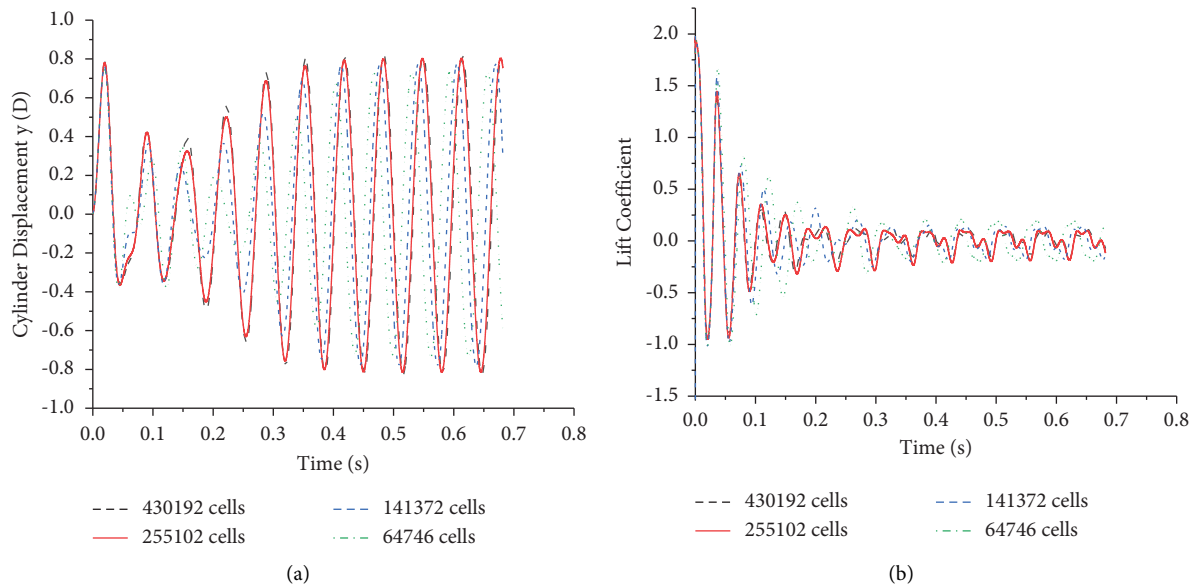


Figure 2: The cylinder dynamic responses (a) and the lift coefficients (b) with different mesh schemes.

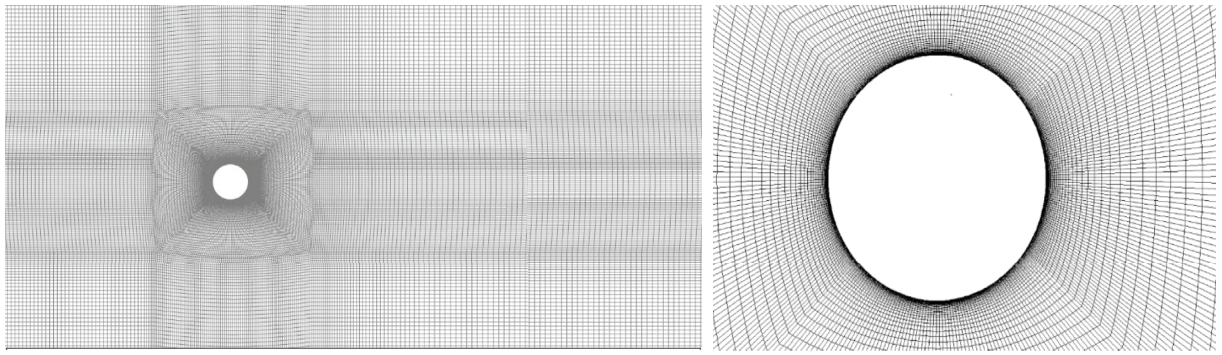

Figure 3: Computational mesh around the cylinder.

$$\dot{y} = w$$
$$\dot{w} = \frac{F(y, \dot{y}, \dot{t})}{m_s}. \tag{10}$$

For a first-order differential equation $\dot{y} = f(t, y)$, the numerical solution is approximated by

$$y_{i+1} = y_i + \frac{1}{24}\Delta t\left(9f_{i+1} + 19f_i - 5f_{i-1} + f_{i-2}\right), \tag{11}$$

where $f_i$ is the value of $f(t, y)$ at $(t_i, y_i)$. Cylinder transverse displacement value was calculated on each time step and transferred to ANSYS Fluent using the incorporated built-in User Defined Function (UDF) mechanism. Based on the calculated cylinder displacement value, Fluent performed the update for the dynamic mesh for each time step. For the solution of mesh displacement, the diffusion method of smoothing was chosen. It was selected because there is simple geometry, linear motion of the rigid body, and a relatively small amplitude of vibrations of the cylinder. The motion of the mesh nodes in the diffusion method is based on the solution of the diffusion equation.

$$\nabla \cdot \left(\gamma \nabla \mathbf{u}_m\right) = 0, \tag{12}$$

where $\mathbf{u}_m$ is mesh displacement velocity and $\gamma$ is the diffusion coefficient, which is determined by the reciprocal of the normalized boundary distance. Based on this equation, a calculation of the mesh cell velocity is performed (velocity at the boundary nodes of the cylinder is used as the Dirichlet boundary condition), and the node positions are then updated according to $\mathbf{x}_{\text{new}} = \mathbf{x}_{\text{old}} + \mathbf{u}_m \Delta t$.

The simulations started with the cylinder at the equilibrium positions, and once the vortex shedding occurred, the cylinder began to move perceptibly. After the calculation

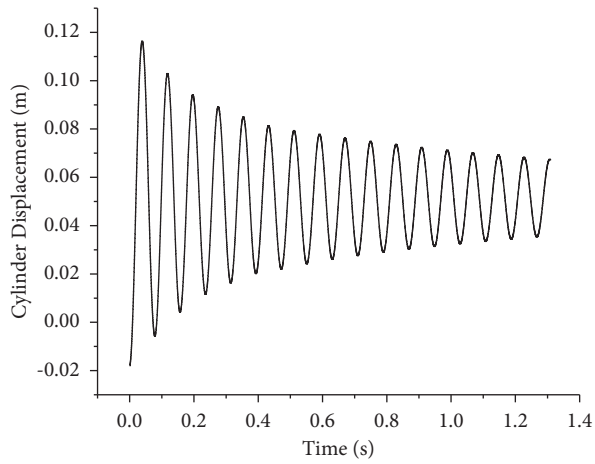


Figure 4: Free vibration of the cylinder in the stationary fluid.

became statistically steady state with the cylinder motion in a periodic manner, the flow data, such as the lift and drag coefficients, and the cylinder displacement were recorded.

## 3. Results

*3.1. The Natural Frequency of the Cylinder Vibration in the Stationary Fluid.* First, the inlet velocity was set small enough so the fluid could be considered stationary. The cylinder is displaced away from the equilibrium position to generate the free vibration. The displacement response is shown in Figure 4, and after examining the period of the free vibration, a natural frequency of 12.2 Hz was found, which corresponds to $f_N = \sqrt{k/(m + m_A)}/2\pi$.

By checking the logarithmic decrement $\delta$ from Figure 4, and using the equation $\delta \approx 2\pi\zeta$ for small damping, we obtained the actual damping ratio $\zeta_{act} = 0.006$, which is a little larger than the predefined experimental value $\zeta = 0.0054$. This is attributed to the fluid viscous damping, i.e., the fluid viscous force over the cylinder behaves as the damping force. In other words, the actual damping coefficient cannot be set a priori since it depends on the fluid viscosity as well as the cylinder vibration.

*3.2. VIV of the Cylinder.* A Fast Fourier transform was applied to the time series data of the cylinder vibration responses. The peak values in the cylinder response spectra with the corresponding frequencies were picked up to analyze the cylinder response characteristics. Figure 5 shows the amplitude response with a comparison of Khalak and Williamson experimental data [14]. As it can be seen, the numerical results agree well with the experimental data in the initial and lower branches. For the upper branch, the numerical simulation predicted a smaller amplitude with $A^*_{max} = 0.66$ obtained, while the flow pattern is similar to the experimental measurement as explained in Section 3.3. The highest amplitude ratio captured is $A^* = 0.67$ at $U_r = 5$ which was reported by Mutlu et al. [25], claiming the results seem better than those from [21] wherein all values of $A^*$ were less than 0.6 with one $A^* = 0.7$ as exception. Kinaci [24] and Mutlu et al. [25] argued that the URANS method cannot

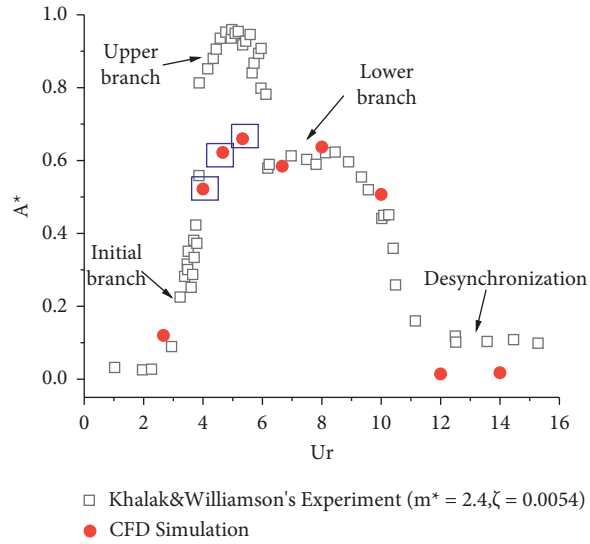


Figure 5: Amplitude response of the cylinder VIV.

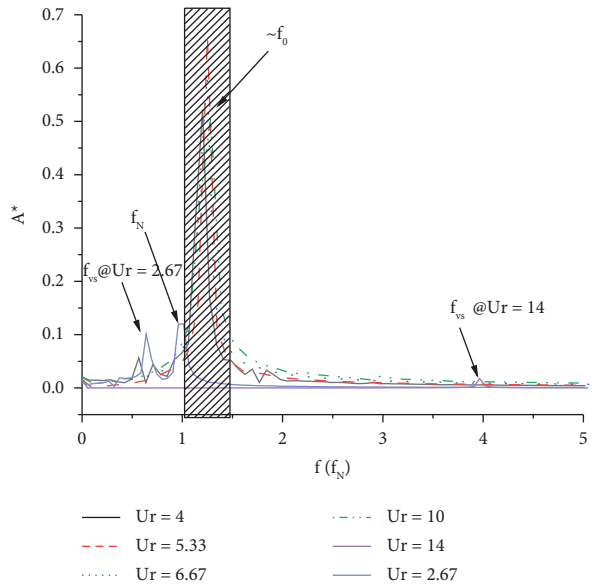


Figure 6: Displacement spectra of the cylinder vibration.

capture the randomness of the vortex-induced vibration in the upper branch due to its implemented averaging algorithm.

Figure 6 shows the displacement response spectra with different reduced velocities. It can be seen clearly that the vibration amplitude increases with the incoming velocity becoming larger, especially in the region of the cylinder vibration resonance where lock-in phenomena occur, and decreases abruptly after a certain value of the reduced velocity $Ur$ when the lock-in disappears. In the case of small $Ur$, the cylinder vibration spectra have two obvious peaks: one is related to the vortex shedding frequency (excitation frequency), and the other is the natural frequency with the added mass $f_N$. With increasing $Ur$, the two peaks merge into a single peak with the frequency around the natural

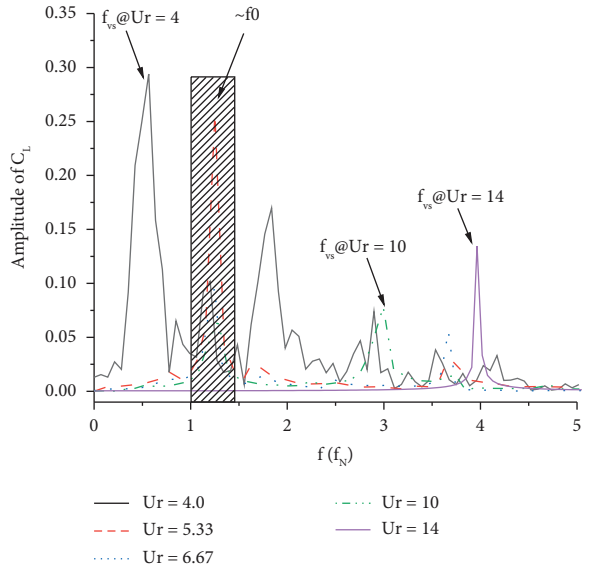


Figure 7: Spectra of lift coefficients.

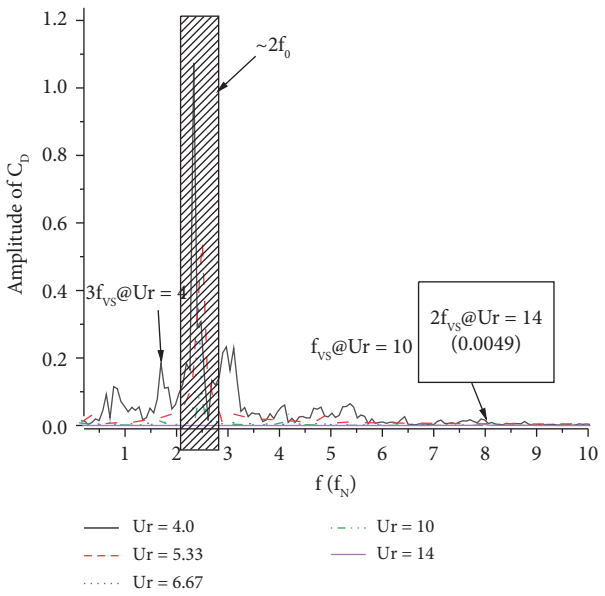


Figure 8: Spectra of drag coefficients.

frequency in vacuum $f_0$. And with a further increase of $Ur$, the cylinder vibration amplitude decreases dramatically, and the corresponding frequency is the vortex shedding frequency $f_{vs}$.

A Fast Fourier transform was applied to the time history data of lift and drag coefficients also, and the spectra are shown in Figures 7 and 8, respectively. The abscissa range of Figure 8 is set to 0.1–10, which is different from 0–5 in Figure 7, considering that the main drag force fluctuations' frequency is two times that of the lift force fluctuations. Also, the drag force has a very large nonzero component at 0 Hz. The frequencies relating to the peak values in the lift spectra are the vortex shedding frequencies since each vortex shedding causes a lift pulsation. Figure 9 shows the overall fluctuations of lift and drag forces versus the reduced

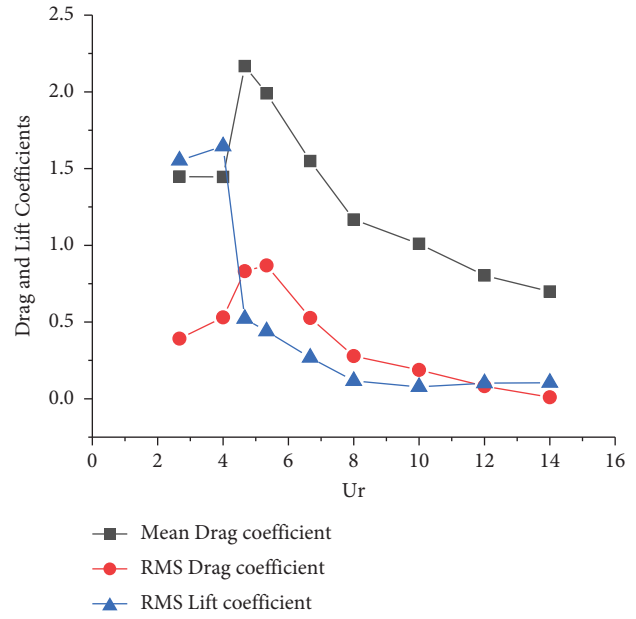


Figure 9: Characteristics of lift and drag coefficients versus reduced velocity.

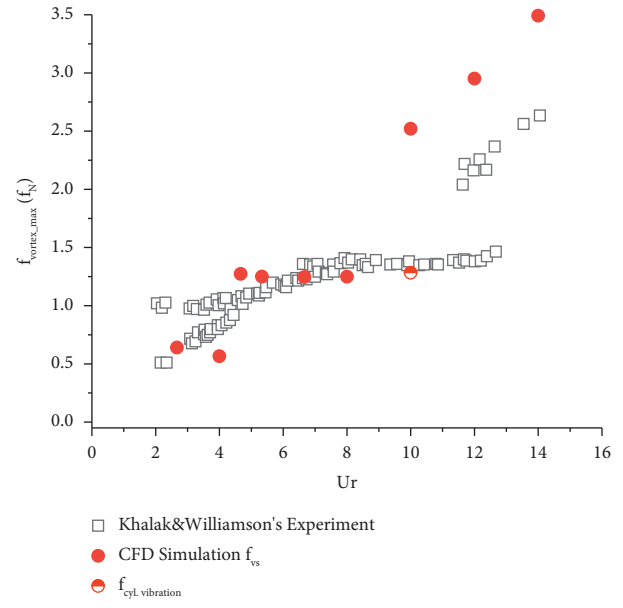


Figure 10: Frequency response through the lock-in regime.

velocity $Ur$, with the root mean square (RMS) value as the indicator. The mean values of the drag coefficient are also shown in Figure 9, while the mean values of the lift coefficient are absent since they are sufficiently low and tend to zero due to statically symmetric flow distribution about the horizontal line through the cylinder equilibrium position.

The vortex shedding frequencies are presented in Figure 10 with the comparison of Khalak and Williamson's experimental data [14] therein. For $Ur = 10$, the peaks at the resonance and at the vortex shedding frequency are

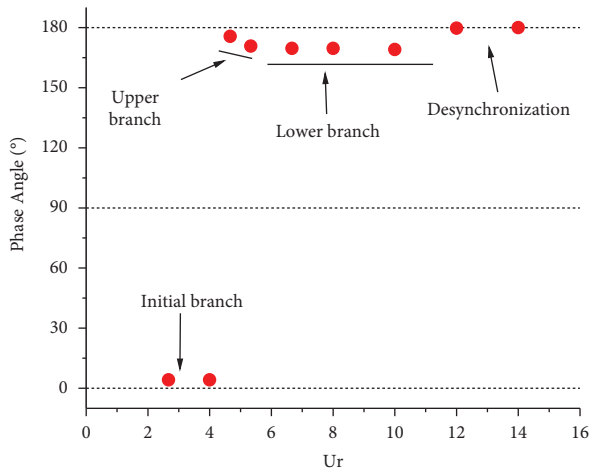


FIGURE 11: Phase angle between the lift force and the cylinder displacement.

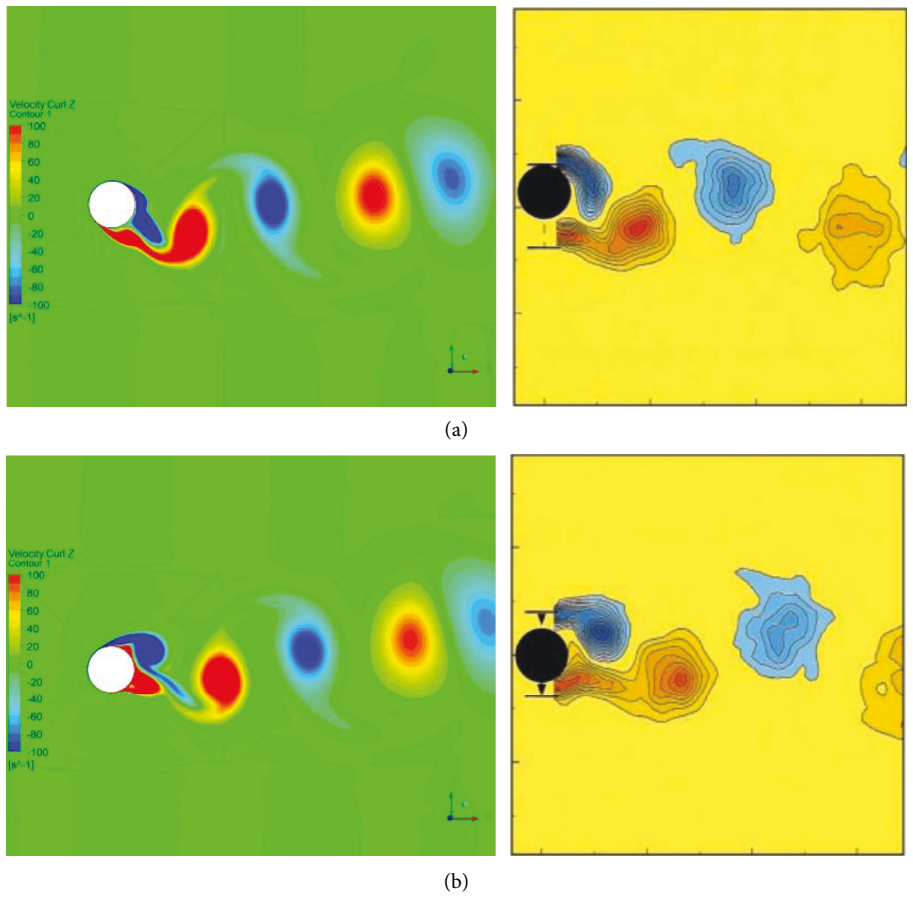


FIGURE 12: Initial branch showing 2S modes of numerical results at $Ur = 2.67$ with $m^* = 2.4$ and $A^* = 0.12$ (left) and PIV measurement results with $= 8.63$ and $A^* = 0.33$ by Govardhan and Williamson [26] (right): (a) cylinder highest position; (b) cylinder zero displacement position when traveling downstream.

comparable, so both frequencies are presented in Figure 10. It can be seen clearly that frequency synchronization (lock-in) occurs in the upper and lower branches.

The phase angle differences $\Delta\varphi$ between the cylinder displacement responses and the lift force at the peak value frequencies are obtained by checking the Fourier spectra. The results are plotted in Figure 11. The conspicuous feature in Figure 11 is the large jump of $\Delta\varphi$ when $Ur$ goes through the upper branch, which was found in experimental studies [10, 13, 26]. It shows the vortex mode transition behind the

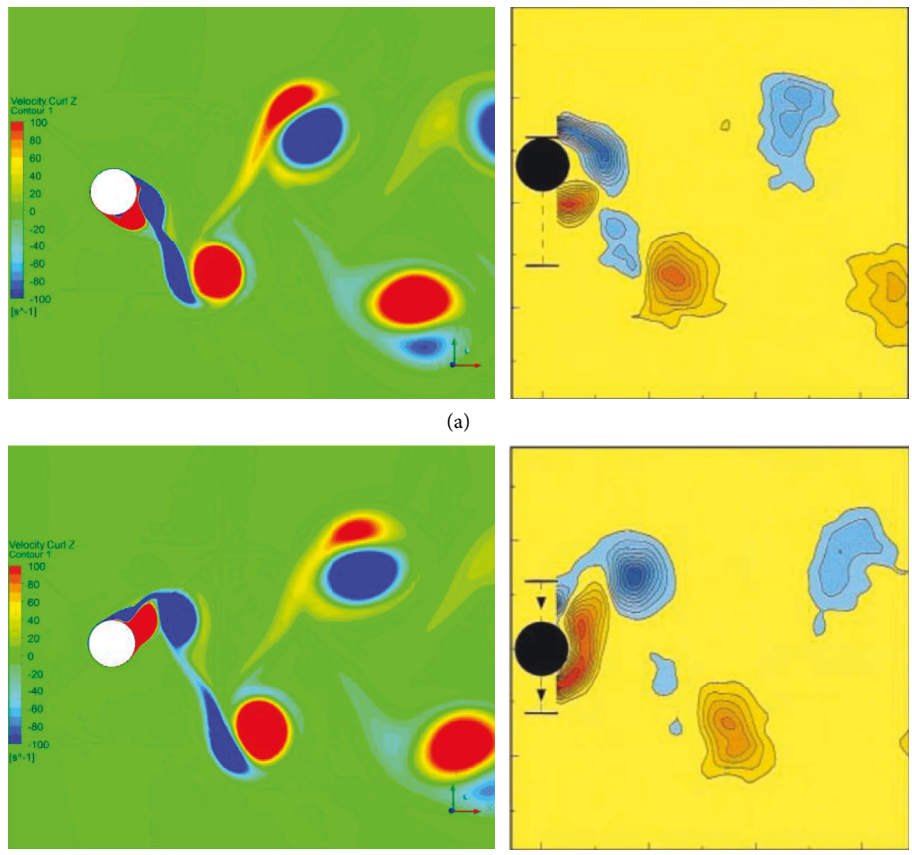


FIGURE 13: Upper branch showing 2P modes of numerical results at $Ur = 4.67$ with $m^* = 2.4$ and $A^* = 0.622$ (left) and PIV measurement results with $m^* = 8.63$ and $A^* = 0.81$ by Govardhan and Williamson [26] (right): (a) cylinder highest position; (b) cylinder zero displacement position when traveling downstream.

cylinder accompanied by the phase jump as discussed in Section 3.3.

*3.3. Vortex Patterns.* The vorticity plots at the initial branch are shown in Figure 12, with the red color vortex (positive value) as the counter-clockwise vortex and the blue one as the clockwise vortex. The vortex pattern behind the cylinder is 2S mode, meaning two single vortices are formed per cycle of the cylinder vibration. The agreement between the numerical and experimental results is reasonable in Figure 12, although the mass ratios are different. This may be due to the fact that at low mass ratios, the cylinder vibration responses in these two cases are comparable, and also the flow regimes are similar with the Reynolds number $Re_D$ less than the critical value. As can be seen, when the cylinder is in the top position, the upper side counter-clockwise vortex around the cylinder is in the process of cutting the down-side clockwise vortex. When the cylinder passes across the equilibrium position from the upper peak position, the clockwise vortex has nearly a point of separation from its boundary layer. Once the separation is complete, a free vortex is formed, and then it is convected downstream by the flow, creating the 2S vortex street.

The vorticity contours of the upper branch are shown in Figure 13, with good agreement with the experimental data. The vortex pattern behind the cylinder is 2P mode, i.e., two pairs of vortices are formed per cycle. As can be seen, in the separation of the down side clockwise vortex, the up side vortex is itself divided into two parts, and one part, together with the free vortex, constitutes the vortex pair. The mechanism of the 2P mode is different from the 2S mode, and this is due to the large cylinder vibration amplitude causing the cutting vortex to be less stable than in the 2S mode case. The vortex plots of the lower branch in Figure 14 also show the 2P mode; however, there is some difference between the vortex modes of the upper and lower branches. The vortices in the vortex pair in the upper branch are much closer to each other, and one vortex is fairly smaller than the other, while in the lower branch, the two vortices are separated by a noticeable distance and the sizes are competitive.

## 4. Discussion

In the present study, the vibration response of the elastically supported cylinder in the cross-flow direction due to VIV with a 2D URANS approach was numerically investigated. From the free vibration result, as judged from Figure 4, the

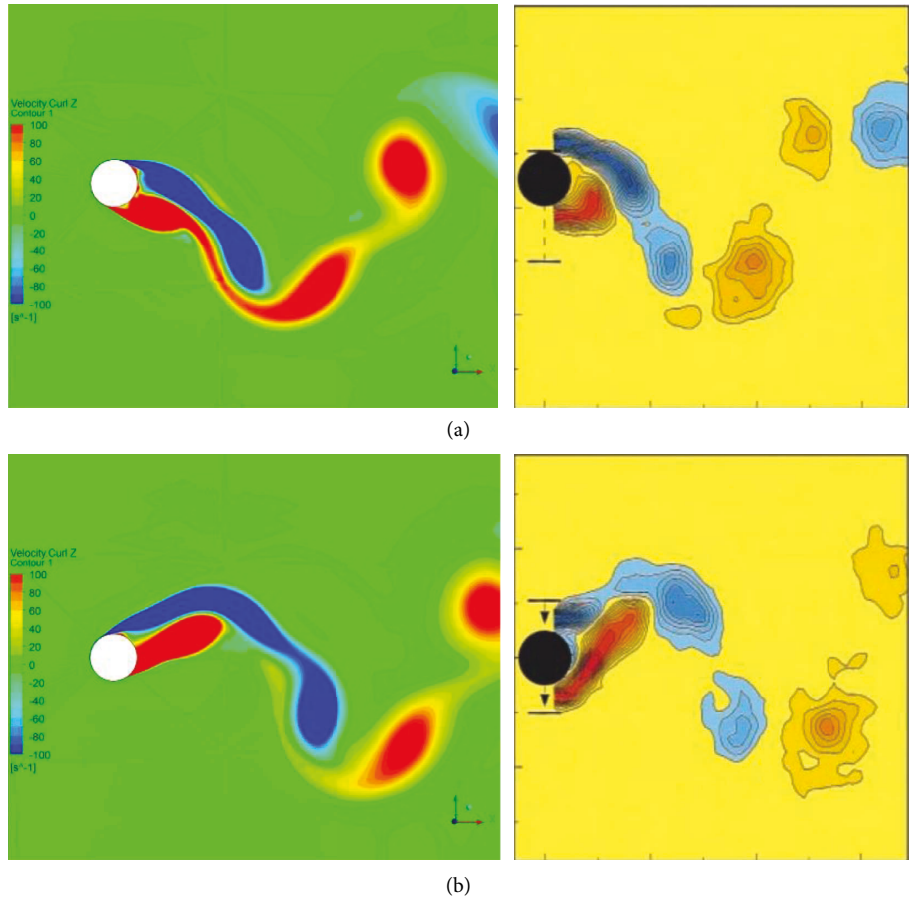


FIGURE 14: Lower branch showing 2P modes of numerical results at $Ur = 8$ with $m^* = 2.4$ and $A^* = 0.637$ (left) and PIV measurement results with $m^* = 8.63$ and $A^* = 0.60$ by Govardhan and Williamson [26] (right): (a) cylinder highest position; (b) cylinder zero displacement position when traveling downstream.

added mass of the fluid is precipitable because the natural frequency is consistent with the equation $f_N = \sqrt{k/(m + m_A)}/2\pi$. From the cylinder displacement spectra in Figure 6, at small reduced velocity $Ur$, the vortex shedding frequency $f_{vs}$ is away from the natural frequency $f_N$ of the cylinder vibration system. The cylinder response has both $f_{vs}$ and $f_N$ components. With the increase of $Ur$, $f_{vs}$ becomes close to $f_N$, and the cylinder vibrations become much more vehement. In the case of large cylinder amplitude, the flow around the cylinder certainly cannot be considered as potential flow. In other words, the added mass from the potential flow theory may not be applicable. As can be seen clearly in Figure 6, there is only one peak in the vibration spectra, whose frequency is the natural frequency in vacuum of $f_0$. Further increasing $Ur$, the cylinder vibration amplitude decreases dramatically with a small peak at the vortex shedding frequency $f_{vs}$.

From the amplitude response Figure 5, the numerical results agree well with the experimental data by Khalak and Williamson experimental data [10], especially the initial and lower branches. For the upper branch, numerical simulation obtained smaller amplitudes. The same result was also found in other numerical studies with 2D approaches, such as [19, 21, 22], except in Guilmineau and Queutey [20], a sufficiently large amplitude was obtained in a very narrow $Ur$ range using very small steps of $Ur$. Kinaci [24] and Mutlu et al. [25] explained that the URANS method cannot capture the nature of the randomness of the vortex-induced vibration in the upper branch due to its implemented averaging algorithm. Nevertheless, in the present study, the flow vorticity distribution behind the cylinder is close to the experimental measurements as shown in Figure 13. The 2P vortex modes in the upper and lower branches by URANS and SST $K$-$\omega$ turbulence model are captured successfully, and the vorticity contour plots are consistent with experimental results. The vorticity distribution of the upper branch shows a more fragmental pattern with the much closer vortices of the 2P pair, while the lower branch has a more connected version of the vortex.

The lift coefficient spectra in Figure 7 show that for low $Ur$ the vortex shedding component $f_{vs}$ is obviously high. Increasing $Ur$ the conspicuous peak is located at $f_0$ indicating a "lock-in" phenomenon, and further increase of $Ur$ results in the peak frequency at $f_{vs}$. For $Ur = 4$, which is in the initial branch and close to the upper branch, the lift and drag spectra are very complex. As can be seen, the lift has a dominating component at the vortex shedding frequency $f_{vs}$., which is different from the cylinder vibration frequency $f_0$, showing lock-in has not occurred yet. By comparing Figure 6, it can be seen that the cylinder vibration amplitude is quite large at $f_0$.

This can induce a certain level of lift force fluctuation at the same frequency. However, the drag force has a prominent peak at the natural frequency of the cylinder vibration system, although some harmonics related to vortex shedding frequency are also noticeable. For the upper and lower branches, lift and drag force spectra have peaks at $f_0$ and $2f_{0,}$ respectively, indicating the frequency lock-in or synchronization happens. For $Ur = 10$, close to the desynchronization, the vortex shedding frequency component in the lift force spectra is also observable. For $Ur = 14$, in the desynchronization due to the small cylinder vibration, the lift and drag forces have only the peaks at the $f_{vs}$ and two times of $f_{vs}$, respectively, showing that the interactions between the vortex shedding and the cylinder motion are negligible.

As it can be seen from Figure 9, the lift force fluctuation increases as $Ur$ approaches the upper branch from the initial branch and decreases gradually when $Ur$ goes down the lower branch to the desynchronization region. While for the drag force, its fluctuation is quite large at the initial branch, and experiences a sharp decline when $Ur$ fully enters the upper branch. Analyzing the lift force coefficient spectra, it is known that in the initial branch, both the vortex shedding and the cylinder vibration have a great influence on the drag force, leading to large fluctuations with different frequencies. However, in the upper and lower branches, the effect of the cylinder vibration on the drag fluctuations is superior. The mean values of the drag coefficient are also shown in Figure 9, and it is interesting to find that its pattern is similar to the RMS lift; i.e., it increases in the upper branch and then decreases in the lower branch and desynchronization region.

The phase angle difference $\Delta\varphi$ between the lift force and the cylinder vibration clearly shows the jump occurring when $Ur$ enters the upper branch from the initial branch, shown in Figure 11. The power input to the cylinder vibration from the fluid flow is closely related to $\Delta\varphi$. The power input equals the product of the lift force and the cylinder velocity in the cross-flow direction, $F_L\dot{y}$. For simple harmonic vibration, the power input value depends on $\cos(\Delta\varphi - 90^\circ)$ considering the velocity phase angle leads the displacement phase angle by 90°.

It can be seen from Figure 11, in the initial branch region, there is a small phase difference between the lift force and the cylinder displacement, which means $\cos(\Delta\varphi - 90^\circ)$ has small values, so that the energy transition from the fluid into the cylinder vibration system is small enough. When $Ur$ goes into the upper and lower branches, $\Delta\varphi$ has certain distance to 180°, so that $\cos(\Delta\varphi - 90^\circ)$ increases substantially, which means fluid energy can be transferred into the vibration system more easily to boost the cylinder vibration. In the desynchronization region, $\Delta\varphi$ is very close to 180°, resulting in a sufficiently small value of $\cos(\Delta\varphi - 90^\circ)$, so that the cylinder vibration amplitude decreases dramatically.

## 5. Conclusions

The vortex-induced vibration (VIV) of an elastically supported cylinder was numerically studied by computational fluid dynamics (CFD). The unsteady Reynolds averaged Navier–Stokes equations (URANS) with the turbulence modelling of shear stress transport (SST) $K$-$\omega$ was applied to calculate the flow fields, and the dynamic mesh approach was used to tackle the domain change due to the cylinder motion.

The characteristics of the amplitude response of the cylinder and the vortex shedding frequency at different reduced velocity were compared with the experimental data, and good agreement was found. The added mass was perceptible in the free vibration and in the initial branch with small cylinder vibration amplitude, while in the upper and lower branches the influence of added mass is weak regarding the fact that the main response frequency of the cylinder is close to the natural frequency in vacuum. Detailed vorticity distributions clearly show the 2P vortex modes at the upper and lower branches and 2S mode in the initial branch.

In the initial branch and close to the upper branch, the lift and drag spectra are very complex with peaks related to both vortex shedding frequency $f_{vs}$ and cylinder dominating vibration frequency $f_0$. For the upper and lower branches, lift and drag forces have peaks at $f_0$ and 2 $f_0$ indicating the frequency lock-in or synchronization happens. In the desynchronization region, which is characterized by the small cylinder vibration, the lift and drag forces have only their peak values at the $f_{vs}$ and $2f_{vs}$, respectively, showing that the interactions between the vortex shedding and the cylinder motion are negligible.

The root mean square (RMS) value of lift force increases as the reduced velocity $Ur$ approaches the upper branch from the initial branch and decreases gradually when $Ur$ goes down the lower branch to the desynchronization region. However, for the drag force, its RMS value is quite large at the initial branch, and experiences a sharp decline when $Ur$ fully enters the upper branch. The pattern of the changes in the mean drag coefficient is similar to that of the RMS lift, i.e., it increases in the upper branch and then decreases in the lower branch and desynchronization region.

The phase difference between the lift force and the cylinder vibration, which influences the power transfer from the flow to the cylinder vibration, was analyzed, and the phase jump was found from the initial branch to the upper branch with the vortex mode switching from 2S to 2P. The difference between the generation mechanisms of the 2S and 2P vortex modes lies in whether the cutting vortex on one side of the cylinder separates into two parts or not. With the large cylinder vibration, the cutting vortex becomes two parts, one part together with the free vortex to form the vortex pair. The 2P modes in the upper and lower branches show some differences. For the upper branch, the vortices in the vortex pair are much closer to each other with one very small vortex, while for the lower branch, the two vortices are separated by a noticeable distance with comparable vortex sizes.

## Data Availability

The data that supports the findings of this study are available within the article.

## Conflicts of Interest

The authors declare no conflicts of interest.

## Authors' Contributions

Xinxing Zhang wrote the original draft and carried out investigation. Minghan Hu contributed to investigation, review, and editing. Jiancheng Cai contributed to writing the original draft, reviewing and editing the draft, funding acquisition, investigation, and methodology. Andrii Babenko carried out the investigation and review and editing. Shiju E carried out the supervision and methodology. Zisheng Xu carried out the supervision, review and editing, and methodology.

## Acknowledgments

The authors acknowledge the supports of th National Natural Science Foundation of China (Grant no. 51976201, 62101498) and Zhejiang Provincial Natural Science Foundation of China (Grant no. LY22E060006).

## References

[1] T. Sarpkaya, "A critical review of the intrinsic nature of vortex-induced vibrations," *Journal of Fluids and Structures*, vol. 19, no. 4, pp. 389–447, 2004.

[2] M. P. Païdoussis, S. J. Price, and E. D. Langre, *Fluid-Structure Interactions: Cross-Flow-Induced Instabilities*, The University of Utah, Salt Lake, UT, USA, 2011.

[3] J. Wang, S. Sun, L. Tang, G. Hu, and J. Liang, "On the use of metasurface for vortex-induced vibration suppression or energy harvesting," *Energy Conversion and Management*, vol. 235, Article ID 113991, 2021.

[4] J. Wang, S. Gu, C. Zhang et al., "Hybrid wind energy scavenging by coupling vortex-induced vibrations and galloping," *Energy Conversion and Management*, vol. 213, Article ID 112835, 2020.

[5] M. Hamlehdar, A. Kasaeian, and M. R. Safaei, "Energy harvesting from fluid flow using piezoelectrics: a critical review," *Renewable Energy*, vol. 143, pp. 1826–1838, 2019.

[6] E. Achenbach, "Distribution of local pressure and skin friction around a circular cylinder in cross-flow up to Re= 5× 106," *Journal of Fluid Mechanics*, vol. 34, no. 4, pp. 625–639, 1968.

[7] E. Achenbach and E. Heinecke, "On vortex shedding from smooth and rough cylinders in the range of Reynolds numbers 6× 103 to 5× 106," *Journal of Fluid Mechanics*, vol. 109, no. 1, pp. 239–251, 1981.

[8] B. Cantwell and D. Coles, "An experimental study of entrainment and transport in the turbulent near wake of a circular cylinder," *Journal of Fluid Mechanics*, vol. 136, pp. 321–374, 1983.

[9] G. . Schewe, "On the force fluctuations acting on a circular cylinder in crossflow from subcritical up to transcritical Reynolds numbers," *Journal of Fluid Mechanics*, vol. 133, no. 1, pp. 265–285, 1983.

[10] B. M. Sumer and J. Fredsoe, "Hydrodynamics around cylindrical structures," *Advanced Series on Ocean Engineering*, World Scientific Publishing Co Pte Ltd, Singapore, 2006.

[11] M. M. Zdravkovich, *Flow Around Circular Cylinders*, Oxford University Press, Oxford, UK, 1997.

[12] M. M. Zdravkovich, *Flow Around Circular Cylinders*, Oxford University Press, Oxford, UK, 2003.

[13] C. Feng, *The Measurement of Vortex-Induced Effects in Flow Past a Stationary and Oscillating Circular and Dsection Cylinders*, Master, University of British Columbia, Vancouver, Canada, 1968.

[14] A. Khalak and C. H. K. Williamson, "Dynamics of a hydroelastic cylinder with very low mass and damping," *Journal of Fluids and Structures*, vol. 10, no. 5, pp. 455–472, 1996.

[15] A. Khalak and C. H. K. Williamson, "Fluid forces and dynamics of a hydroelastic structure with very low mass and damping," *Journal of Fluids and Structures*, vol. 11, no. 8, pp. 973–982, 1997.

[16] A. Khalak and C. H. K. Williamson, "Motions, forces and mode transitions in vortex-induced vibrations at low mass-damping," *Journal of Fluids and Structures*, vol. 13, no. 7-8, pp. 813–851, 1999.

[17] A. Khalak and C. H. K. Williamson, "Investigation of relative effects of mass and damping in vortex-induced vibration of a circular cylinder," *Journal of Wind Engineering and Industrial Aerodynamics*, vol. 69–71, pp. 341–350, 1997.

[18] M. H. Bahmani and M. H. Akbari, "Effects of mass and damping ratios on viv of a circular cylinder," *Ocean Engineering*, vol. 37, no. 5-6, pp. 511–519, 2010.

[19] W. Li, J. Li, and S. Liu, "Numerical simulation of vortex-induced vibration of a circular cylinder at low mass and damping with different turbulent models," in *Proceedings of the Paper presented at the OCEANS 2014 - TAIPEI*, Taipei, Taiwan, April 2014.

[20] E. Guilmineau and P. Queutey, "Numerical simulation of vortex-induced vibration of a circular cylinder with low mass-damping in a turbulent flow," *Journal of Fluids and Structures*, vol. 19, no. 4, pp. 449–466, 2004.

[21] Z. Y. Pan, W. C. Cui, and Q. M. Miao, "Numerical simulation of vortex-induced vibration of a circular cylinder at low mass-damping using rans code," *Journal of Fluids and Structures*, vol. 23, no. 1, pp. 23–37, 2007.

[22] N. B. Khan, Z. Ibrahim, M. I. Khan, T. Hayat, and M. F. Javed, "Viv study of an elastically mounted cylinder having low mass-damping ratio using rans model," *International Journal of Heat and Mass Transfer*, vol. 121, pp. 309–314, 2018.

[23] H. Sayyaadi and A. Motekallem, "Numerical simulation of vortex induced vibration of three cylinders in regular triangle Arrangement at high Reynolds number," in *Proceedings of the Seventh Asia-Pacific Conference on 2016*, Taipei, Taiwan, November 2016.

[24] O. K. Kinaci, "2-D urans simulations of vortex induced vibrations of circular cylinder at Trsl3 flow regime," *Journal of Applied Fluid Mechanics*, vol. 9, no. 7, pp. 2537–2544, 2016.

[25] A. O. Mutlu, M. Bayraktar, and S. Bayraktar, "Two-dimensional simulations of vortex-induced vibration of a circular cylinder," *Proceedings of the Institution of Mechanical Engineers - Part M: Journal of Engineering for the Maritime Environment*, vol. 235, no. 3, pp. 683–694, 2021.

[26] R. Govardhan and C. H. K. Williamson, "Modes of vortex formation and frequency response of a freely vibrating cylinder," *Journal of Fluid Mechanics*, vol. 420, pp. 85–130, 2000.

[27] F. R. Menter, M. Kuntz, and R. Langtry, Eds., *Turbulence Heat & Mass Transfer*, Begell House Inc, Redding, CT, USA, 2003.
[28] J. H. Ferziger, M. Perić, and R. L. Street, *Computational Methods for Fluid Dynamics*, Springer, Berlin, Germany, 2020.
[29] I. B. Celik, U. Ghia, P. J. Roache, C. J. Freitas, H. Coleman, and P. E. Raad, "Procedure for estimation and reporting of uncertainty due to discretization in cfd applications," *Journal of Fluids Engineering*, vol. 130, p. 7, 2008.
[30] R. S. Esfandiari, *Numerical Methods for Engineers and Scientists Using Matlab*, CRC Press, Boca Raton, FA, USA, 2017.